IL NUOVO CIMENTO Vol. 31 C, N. 5-6 Settembre-Dicembre 2008
DOI 10.1393/ncc/i2009-10349-0

Multifractal observations of eddies, oil spills and natural slicks in the ocean surface

A. Platonov(1), A. Carrillo(1), A. Matulka(1), E. Sekula(1), J. Grau(1), J. M. Redondo(1)(*) and A. M. Tarquis(2)

(1) *Departamento de Fisica Aplicada, Universitat Politecnica de Catalunya - B5 UPC Campus Nord, Barcelona, 08034, Spain*
(2) *Departamento de Matemática Aplicada a la Ingeniería Agronómica E.T.S. de Ingenieros Agrónomos, U.P.M. Ciudad Universitaria s.n. - Madrid 28040, Spain*

(ricevuto il 10 Novembre 2008; approvato il 30 Marzo 2009; pubblicato online il 25 Giugno 2009)

Summary. — Natural and man-made distributions of tensioactive substance concentrations in the sea surface features exhibit self-similarity at all radar reflectivity levels when illuminated by SAR. This allows the investigation of the traces produced by vortices and other features in the ocean surface. The man-made oil spills besides often presenting some linear axis of the pollutant concentration produced by moving ships also show their artificial production in the sea surface by the reduced range of scales, which widens as time measured in terms of the local eddy diffusivity distorts the shape of the oil spills. Thanks to this, multifractal analysis of the different backscattered intensity levels in SAR imagery can be used to distinguish between natural and man-made sea surface features due to their distinct self-similar properties. The differences are detected using the multifractal box-counting algorithm on different sets of SAR images giving also information on the age of the spills. Different multifractal algorithms are compared presenting the differences in scaling as a function of some physical generating process such as the locality or the spectral energy cascade.

PACS 92.10.Sx – Coastal, estuarine, and near shore processes.
PACS 93.85.Bc – Computational methods and data processing, data acquisition and storage.

1. – Introduction

Most mixing processes in the ocean depend both on advection and diffusion characteristics with energetic inputs at many different scales, the topology of tracers in the ocean surface probable depends on the local characteristics of the turbulent cascades.

(*) E-mail: redondo@fa.upc.edu

For example, in the detected vortices in the ocean, local shear will transform slicks in the surface to align and follow the local flow so the resulting pattern is spiral as shown by Munk [1]. The mixing processes at large scale produce stirring, which maintains large gradients of the tracers. But in order to mix at molecular level in an irreversible fashion, the energy has to cascade to the smallest internal scales (Kolmogorov or Batchelor scales).

An important topological tool, fractal analysis was pioneered by Richardson and popularized by Mandelbrot. The fractal dimension is a very useful indicator of the complex environmental flow dynamics [2,3], but it only reflects the self-similar geometry, not the dynamics of the flow. Because the oceans receive energy inputs at a wide range of scales, and the non-linear interactions that follow produce turbulent cascades of the type described by Richardson and Kolmogorov [4-6] (3D) and Kraichnan [7] (2D). The characteristics of these turbulent cascades, which may be assumed to conserve energy, energy dissipation, enstrophy, enstrophy dissipation or helicity, will affect the dispersion of the pollutants as well as the natural tracers in the ocean surface.

The ability of the SAR equipped satellites to monitor a large sea area and the fact that radar reflections are sensible to either surface tension-actives or pollutants that change the sea surface roughness make them an important tool in environmental research. Man-made oil/water wash spills dampen the small-scale surface waves, these in turn are responsible for the radar backscattering from the water surface, and are clearly visible as dark patches or lines in SAR images (fig. 1) that most times strike out from the rest of the image. Other types of oceanic and atmospheric phenomena also cause specific signatures due to changes in the surface capillary waves similar to those due to oil slicks. These features are advected by the local currents so they are also able to reveal the structure of the ocean surface [8-10]. It is important to point out that the detection ability of oceanic surface films by SAR sensors strongly depends on wind speed: at either very low wind speeds (below approximately 2 m/s) or very high wind speed (above approximately 10 m/s) oceanic surface films cannot, or may only barely, be identified [10-13]. On the other hand, the sunshine illumination conditions are not a limiting factor for the acquisition of SAR images as the cloud cover is transparent for SAR sensors. The nocturnal conditions are not limiting either because SAR is an active sensor that radiates its own energy.

These effects allow us to use remote sensing of the ocean surface even to monitor and police pollution from space. Here we will discuss several techniques that are able to extract geometrical information from the ocean surface linked in several ways to the dynamics of a certain area. Multifractal analysis is useful on different accounts as a quantitative technique to distinguish the origin of several features.

Oceanic and atmospheric flows may be considered as turbulent motions under the constraints of geometry, stratification and rotation. At large scales these flows tend to occur mostly along isopycnal surfaces due to the combined effects of the very low aspect ratio of the flows (the motion is confined to thin layers of fluid) and the existence of stable density stratification. The effect of the Earth's rotation is to reduce the vertical shear in these almost planar flows. The combined effects of these constraints are to produce approximately two-dimensional turbulent flows termed as geophysical turbulence.

2. – Geophysical turbulence

In a strictly two-dimensional flow with weak dissipation, energy input at a given scale is transferred to larger scales, because these constraints stop vortex lines being stretched or twisted. Physically this upscale energy transfer occurs by merging of vortices and leads

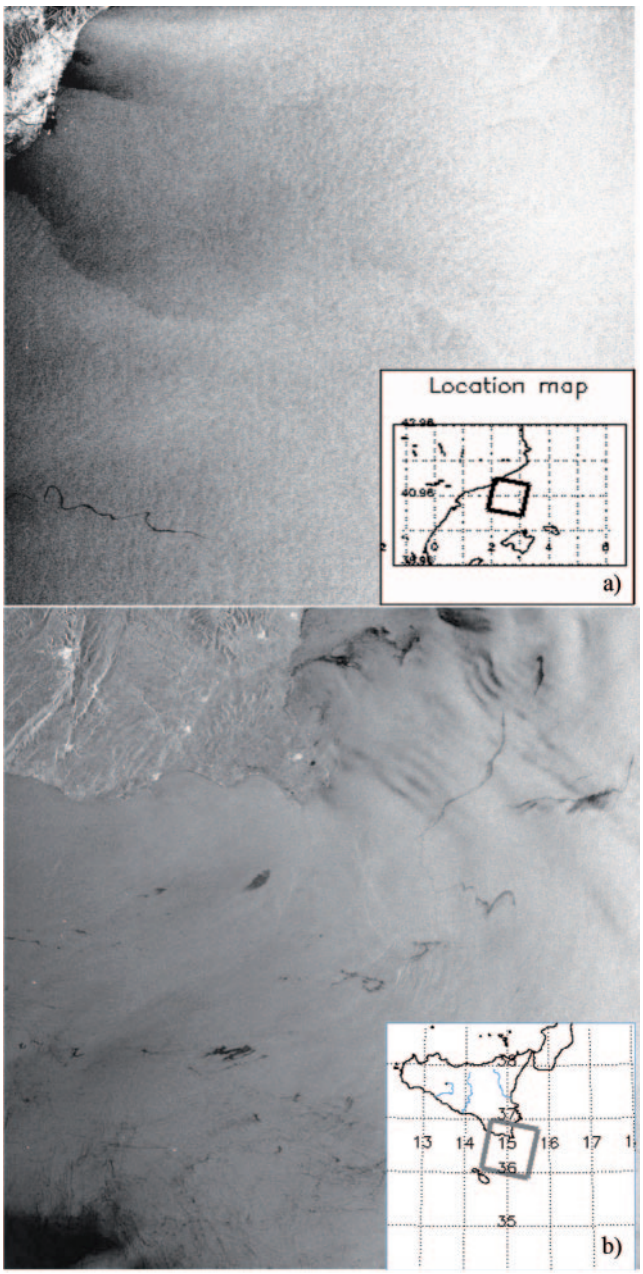

Fig. 1. – a) Example of ERS-2 SAR images (left) with a recent oil spill in the north-western Mediterranean near Barcelona. b) Multiple spills near Sicily; the image's box sizes are approximately 100 km.

to the production of coherent structures in the flow that contain most of the energy. This process generates the appearance of order from chaos [14, 15].

This scenario is an appropriate model for geophysical flows which are known to contain

very energetic vortices mesoscale oceanic eddies and atmospheric highs and lows. This upscale transfer of energy is inhibited at the Rossby deformation radius:

$$L_R = \frac{N}{f} h,$$

where h is the characteristic scale of the depth of the thermocline, N the Brunt-Väisälä frequency and f the Coriolis parameter.

The energy limitation is caused by baroclinic instability at larger scales, which accounts for the dominant observed size of geophysical vortices detected in laboratory experiments on annulus flow, where the flow is driven in a rotating annulus by differential heating of the lateral walls of the annulus, or by internal heating of the fluid. A horizontal temperature gradient is established which drives a zonal flow via the "thermal wind" balance. For certain values of the parameters this flow is unstable to baroclinic modes that feed on the energy in the temperature or density fields.

Many features have been identified with structures and phenomena observed in several experiments, and understanding of atmospheric and ocean dynamics has been significantly advanced. The experiments have provided new insights about the dynamics and have revealed a wide range of nonlinear behaviours.

Experiments performed by Linden *et al.* [15] showed the effect of mixing from the edge on a rotating stratified system. When the instability is caused by differential heating or by buoyancy there seems to be a range of very different dynamic regimes. Work by Carrillo [16] has revealed the possible complex interactions between lateral (or coastal) stirring and the rotating-stratified flow dynamics.

The investigation of such strongly non-homogeneous flow, which leads to intermittent two-dimensional turbulence [17,18] is believed to be very important if correct parameterizations of pollutant dispersion (such as Oil spills) in coastal areas are to be made. The availability of a large-scale flow allows both to measure Eulerian velocities with precision as well as Lagrangian flows using particle tracking as well as local measurements of diffusivity by video recording the dispersion of neutral tracers. A possible oil spill prediction technique involves the releasing of hundreds of small and inexpensive tracer (GPS) Lagrangian buoys near an accident to aid the predictions of coastal currents [12, 13].

Recent man-made oil spills in the sea surface are characterized by the low fractal dimension values ($D < 1.2$) over the region of low reflectivity in SAR images, on the other hand, natural oil slicks show a typical parabolic shape with a maximum of $D < 1.5$. Most of the SAR images analyzed were obtained during 1996-1998 (near 900 images of European coastal waters with 300 in the NW Mediterranean Sea area) but SAR and ASAR images from ENVISAR have also been used. One of the problems in order to identify oil spills is the possibility of confusion with natural tensioactive spills, which may be due to plankton, algae or even wind pattern reflections on the ocean surface, one of the possibilities is to use the scaling properties of the turbulence that advects and diffuses the tracers [19, 20].

3. – Multifractal objects and fractal dimensions

Fractals are geometric entities that present self-similarity and they are often the result of iterative processes such as turbulence. The self-similarity implies that if we accomplish observations from different scales the results are similar, although in natural systems it is enough to have only a certain statistical similarity. These entities have usually anisotropic

nature and then there may be different scaling laws for the different directions. Examples of these are the surface topography and the clouds, where the vertical coordinate has a smaller magnitude than horizontal coordinates due to stratification. Fractal analysis is a very useful tool to characterize these objects in which an additional possibility is the calculation of the corresponding fractal dimension along the different coordinates so it may also reflect the anisotropic scaling [21, 22].

3˙1. *Fractal scalar fields*. – The theory applied here links fractal analysis to the turbulence self-similarity [22-24]. Turbulent diffusivities and Richardson's law applied to the ocean surface probed by the SAR images will be discussed. If we consider the variance of a special signal, then

$$V(\lambda) = V(0) - \frac{S^2(\lambda)}{2} = \langle(\rho(x+\lambda)\rho(x))^2\rangle. \tag{1}$$

The self-similar character of the signal, that for velocity differences, including intermittency, was popularized in [6, 21] through the use of structure functions may scale through the Hausdorff dimension H when the limit

$$\lim_{\lambda\to 0} \frac{\langle(\rho(x+\lambda) - \rho(x))\rangle}{\lambda^H} \tag{2}$$

converges and then the dependence corresponds to a fractal set, either in space or in the form of a time series (when the coordinate is time and instead of a wave-number we have a period).

With the stated conditions, the variance of the signal under study will show a scale dependence such that $V(\lambda) \approx \lambda 2H$ [22-25].

Using $\lambda = 2\pi/k$ and the description of the spatial spectral density function, $E(k)$, we have

$$E(\lambda) \approx \lambda^{\beta} \tag{3}$$

and relating the scalar equivalent to the turbulence energy spectrum as a Fourier transform of the correlation, also directly related to the second-order structure function as

$$S^2(x,\lambda) = \langle\rho^2(x,\lambda)\rangle = V - \frac{1}{2}\left\langle(\rho(x+\lambda) - \rho(x))^2\right\rangle. \tag{4}$$

We may write in terms of the spatial equivalent to the turbulent energy density

$$E(k)\,\alpha\,\lambda \int_0^{\lambda} \rho^2(x)\, e^{ikx}\,\mathrm{d}x \approx \lambda V \tag{5}$$

so relating the Euclidean, fractal and Hausdorff dimensions, using $(H = E - D)$ [2]

$$E(k) \;\approx\; \lambda V \approx \lambda^{2H+1} \approx \lambda^{2E+1-2D}. \tag{6}$$

Thus the relationship between the exponent of the spectral density function and the maximum fractal dimension may be written as

$$\beta = 2E + 1 - 2D \tag{7}$$

and inversely

$$D = E + \frac{1-\beta}{2}\,. \tag{8}$$

These relationships may be used to relate the maximum fractal dimension of a spatial signal to the spectral power slope (including intermittency) of the environment. If the signal used is the SAR radar intensity D would reflect the ocean surface type of horizontal turbulent cascade assuming that the tensioactive tracers act in a passive way being advected by the velocity field.

3˙2. *Theory of multifractal measurements.* – The measurement of multifractals is mainly the measurement of a statistic distribution which is why the results yield useful information even if the underlying structure does not show a self-similar or self-affine behavior as shown by Plotnick *et al.* [26].

For a monofractal object, as mentioned above, the number n of features of a certain size δ varies as

$$n(\delta) \propto \delta^{-D_0}, \tag{9}$$

where the fractal dimension D_0

$$D_0 = \lim_{\delta \to 0} \frac{\log n(\delta)}{\log \dfrac{1}{\delta}} \tag{10}$$

can be measured by counting the number n of boxes needed to cover the object under investigation for increasing box sizes δ and estimating the slope of a log-log plot.

There are several methods for implementing multifractal analysis; in this section the moment method [2, 3] is explained. This method uses mainly three functions: $\tau(q)$, called the mass exponent function, α, which is known as the coarse Hölder exponent, and finally the function $f(\alpha)$, or multifractal spectrum. For a measure (or field) defined in a two-dimensional support of the $L \times L$ pixels image, μ (may be considered as the grey tone from 0 to 255 in a normal 8 bit image), it could be spatially decomposed in terms of infinitely many intertwined sets of fractal dimensions. If that is the case, one fractal dimension cannot characterize all the complexity and several fractal dimensions will be estimated depending on the position. Applying box-counting "up-scaling" partitioning process we can get the partition function $\chi(q, \delta)$ defined as [3]

$$\chi(q, \delta) = \sum_{i=1}^{n(\delta)} \mu_i^q(\delta) = \sum_{i=1}^{n(\delta)} m_i^q, \tag{11}$$

where m is the mass of the measure, q is the mass exponent, δ is the length size of the box and $n(\delta)$ is the number of boxes in which $m_i > 0$. Based on this, the mass exponent function ($\tau(q)$) shows how the moments of the measure scale with the box size:

$$\langle \tau(q) \rangle = \lim_{\delta \to 0} \frac{\log \langle \chi(q, \delta) \rangle}{\log(\delta)} = \lim_{\delta \to 0} \frac{\log \left\langle \sum_{i=1}^{n(\delta)} m_i^q \right\rangle}{\log(\delta)}\,, \tag{12}$$

where $\langle\ \rangle$ represents the statistical moment of the measure $\mu_i(\delta)$ defined on a group of non-overlapping boxes of the same size partitioning the area studied. D_q are related as $\tau(q) = (1-q)D_q$.

This characterization of multifractal measures is the concept of generalized dimensions D_q, which corresponds to the scaling exponents for the q-th moment of the measure. Based on the work of Rényi [27] they are defined as

$$D_q = \lim_{\delta \to 0} \frac{1}{1-q} \frac{\log \sum_{i=1}^{n(\delta)} {m_i}^q}{\log \delta}\,. \tag{13}$$

The sum in the numerator of eq. (5) is dominated by the highest values of m_i for $q > 0$, and by the lowest values of m_i for $q < 0$.

The singularity index (α) can be determined by Legendre transformation of the $\tau(q)$ curve [25] as

$$\langle \alpha(q) \rangle = \frac{\mathrm{d}\langle \tau(q) \rangle}{\mathrm{d}q}\,. \tag{14}$$

The number of cells of size δ with the same α, $n_\alpha(\delta)$, is related to the cell size as $n_\alpha(\delta) \propto \delta^{-f(\alpha)}$, where $f(\alpha)$ is a scaling exponent of the cells with common α. The parameter $f(\alpha)$ can be calculated as

$$\langle f(\alpha) \rangle = q\langle \alpha(q) \rangle - \langle \tau(q) \rangle. \tag{15}$$

Multifractal spectrum (MFS), a graph of α *vs.* $f(\alpha)$, quantitatively characterizes variability of the measure studied with asymmetry to the right and left indicating domination of small and large values, respectively. The width of the MF spectrum indicates overall variability.

MFA in 2D images involves partitioning the plane into boxes to construct samples with multiple scales. The box-counting (BC) method combines pixels to form larger mutually exclusive boxes each containing different sets of pixels. If we have an image of $L \times L$ pixels and a partitioned process is applied with a box size $\delta \times \delta$, then the number of boxes with linear size $\delta(n(\delta))$ will follow the proportion:

$$n(\delta) \propto \left(\frac{L}{\delta}\right)^2. \tag{16}$$

The larger is δ the larger the number of samples needed to carry out a convergent statistical analysis.

As examples of the image enhancement and of the techniques used to reveal the structure of the oil slicks and spills detected by the reduction in surface roughness of the ocean, fig. 2 shows an enhanced SAR image with two typical examples where a combination of oil spills and natural slicks is present; in fig. 3 the same information given by the spatial distribution of SAR intensity pixels (about $4 \times 10^4\,\mathrm{m}^2$ per pixel) in a 3D representation, with the third coordinate indicating the actual local value of the SAR intensity.

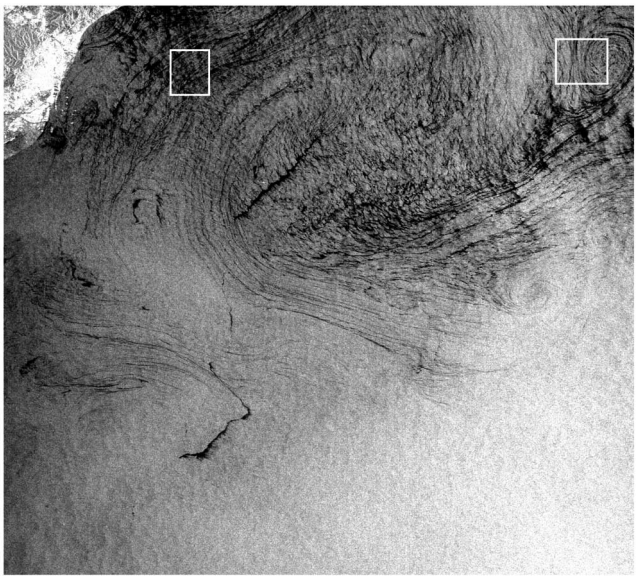

Fig. 2. – SAR ERS-2 images of the area near Barcelona 24.08.97, marked squares show the regions of image enhancement (oil spill (left) and self-similar vertical surface feature (right)) as shown in fig. 8.

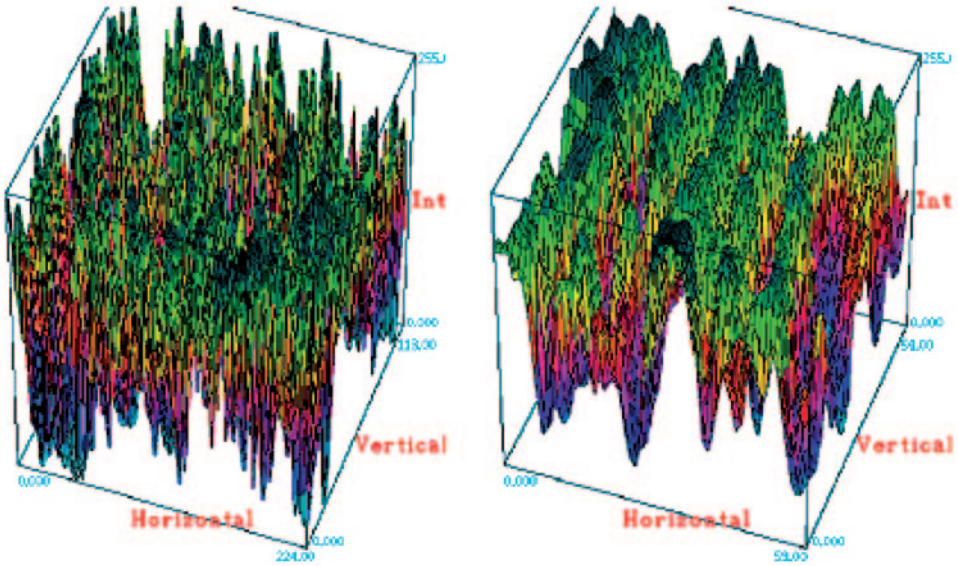

Fig. 3. – Analyzed by DigImage the results of 3D structure of the false colour derived from intensity of SAR signals that reflect surface roughness: oil spill (left) and self-similar vertical surface feature (right).

3˙3. *Multifractal measurements*. – To calculate the fractal dimension, the box-counting method used produces a coverage of the object as discussed above. For the plane these boxes will be squares and for an object in space they will be cubes. The distribution of the boxes is accomplished systematically, the intersection of these with the object carries the fact that we have N boxes with a non-void intersection, but as they are not exactly the result of the better coverage possible, the concept of self-similarity may be applied and thus the basic covering is accomplished repeating the process for many different possible diminishing observation scales.

When we work with real images they do not have generally some perfectly defined contours, but we have some wide quite ranges of scalar intensity values to process. If we group the available data and describe them by a single large set and calculate the fractal dimension, we then lose the corresponding information due to the intensity variation.

It is also possible to accomplish a segmentation in many intervals that contains each one a very well-defined intensity range. For each one of these ranges the usual fractal dimension calculation with the box-counting method will be applied and we will obtain the corresponding fractal dimension for each intensity level. The result of the process will be a set of dimension values, function of the intensity, and this measure will not need to rely on the evaluation of a limit neither to the smallest nor to the largest scales. An advantage of this straightforward method is that the best fit to calculate D may be performed choosing freely the scale, the scale interval and the number of pixel values that will be used.

The fractal dimension $D(\rho)$ is then a function of pixel intensity (we may relate μ to ρ) and may be calculated using

$$D(\rho) = -\frac{\log N(\rho)}{\log \lambda}\,, \tag{17}$$

where $N(\rho)$ is the number of boxes of size λ needed to cover the SAR contour of intensity ρ.

The box-counting algorithm divides the embedding Euclidean plane in smaller and smaller boxes (*e.g.*, by dividing the initial length λ_0 by n, which is the recurrence level of the iteration). For each box of size λ_0/n it is then decided if the convoluted line, which is analyzed, is intersecting that box. Finally, N *versus* λ_0/n (*i.e.* the size of the box e) in a log-log plot is plotted, and the slope of that curve, within reasonable experimental limits, gives the fractal dimension. This method of box-counting is used in ImaCalc software [10] that we applied to detect the self-similar characteristics for different SAR image grey intensity levels ρ and to identify different sea surface dynamic processes. Each of the intensity values may reflect different physical processes and lead to a different value of its fractal dimension, this whole entity can be either fractal or non-fractal but exhibits a range of values 0–2 for each intensity.

The program ImaCalc [10-13] performs interactively most of the multifractal box-counting methods as well as the spectral ones. Different regions may be equalized depending on their intensity histogram distribution. Figure 4 shows the dialog box with the zoom, histogram and a fractal fit. With this application we can define the image region of interest, select an intensity range to analyze and execute the multifractal characterization process in a simple iterative way. On the right side of fig. 4, other smaller boxes show the observed dimension values as a grey-level function of the characterized intervals, which may also be selected.

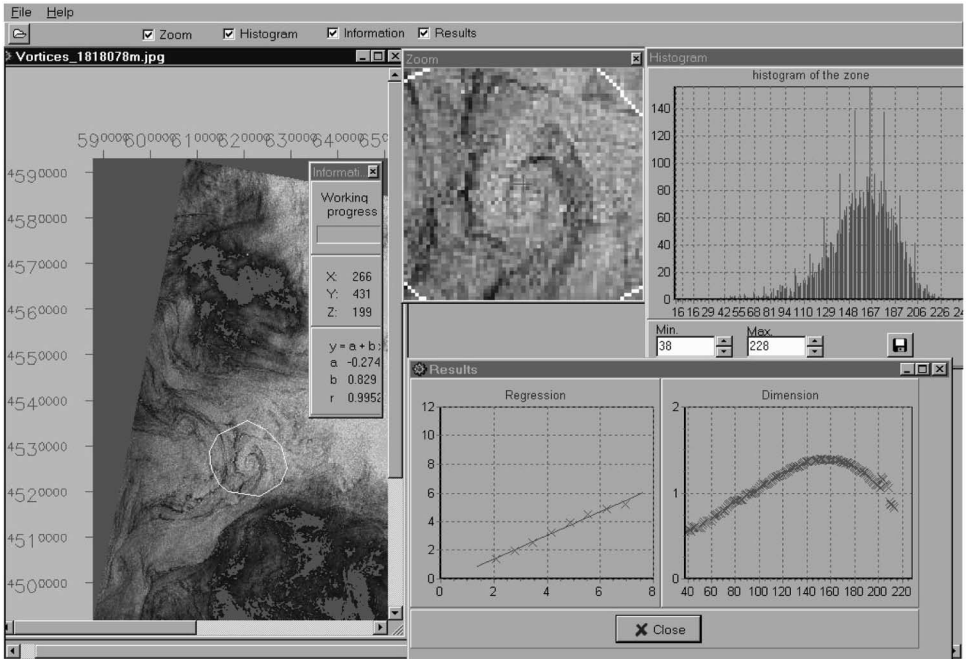

Fig. 4. – Example of the use of ImaCalc on a ERS-1 SAR image with surface features showing a vortex in the Northwest Mediterranean near Barcelona.

Using the traditional energy spectra used in turbulence studies characterized by a single power law within the inertial sub-range (defined as the range of scales where production and dissipation of energy, ε are in local balance) we may use a theoretical relationship between the turbulence spectral slope and the fractal dimension, we are now able to apply it to a spatial spectrum as described above, and define a global fractal dimension using directly the spectral analysis on the radial distribution of intensity values of a SAR image.

With this methodology a unique value is obtained that characterizes the overall spatial fractal dimension of the system. The steps are described as follows [23]: make an image segmentation to obtain the interest region. (ρ_{mn}, m and n are the x-y discrete coordinates.) Compute the FT (Fourier Transform) to obtain the frequency spectrum representation. (I_{uv}, u and v are the frequency discrete coordinates.) Compute the square of the signal intensity or energy S_{uv} with: $S_{uv} = |\rho_{uv}|^2$. Obtain the *radial* representation, as the radial distribution of S_{uv} and finally find the exponent β from $S_r = r^{-\beta}$. Using the radius as an isotropic length scale λ.

With a linear fit from a log-log representation of S_r we may obtain the spatial spectral value of the set of all SAR image intensities, which we assume is also β and using as the Euclidean dimension $E = 3$ and the fractal dimension relationship we have

$$D = \frac{7 - \beta}{2}\,. \tag{18}$$

And thus we also have a global, indirect measure of the average fractal dimension from the radial spectral energy, note that only if the scalar used corresponds to a velocity com-

ponent energy will have the correct physical dimension, otherwise the energy spectrum will just indicate the square of the physical signal used.

4. – Results

The measurement of multifractals is mainly the measurement of a statistic distribution which is why the results yield useful information even if the underlying structure does not show a self-similar or self-affine behaviour. For a monofractal object, the number N of features of a certain size e varies as can be measured by counting the number N of boxes needed to cover the object under investigation for increasing box sizes e and estimating the slope of a log-log plot. For multifractal measurements, a probability distribution is measured. In practice, using the box-counting method, for every box i the probability of "containing the object", or in this application, the values of a certain SAR reflectivity, is also called the partition function, which may be obtained for different moments q which can vary from -8 to $+8$. Both methods described above may be used to extract useful information about the age of the oil spills as well as about other mixing processes in the oceal surface.

Thus it is possible to define D as described above. The well-known [24-28] multifractal function $f(a)$ may be seen as the fractal dimension of the set of intervals that corresponds to a singularity a, and a graph of a *vs.* $f(a)$ is called the multifractal spectrum of the measure. A measure is multifractal when its multifractal spectrum exists and has the shape of an inverted parabola. A generally equivalent way to describe a multifractal scaling is by considering the scaling laws of the moments of the measure.

In practice, the object density is taken to the respective power of q, summed for all i, and plotted *versus* the box size in a log-log coordinate system. From the slope, which is also called the mass exponent t, the generalized dimensions are estimated as $D(q) = t(q)/(1-q)$.

Images can be pre-processed using any image processor, *e.g.*, to convert from colour/grey images to black-and-white using different types of algorithms, to invert background and foreground, to extract boundaries. With SAR images from the ocean surface we cannot rely strictly on theoretical limit for the calculation of the fractal, non-fractal or multifractal behaviour, because they have a finite size, and we have assigned a fixed range of values to the different SAR reflectivity intensity. The ranges of scale boundaries are defined by the image resolution, and we use numerical log/log fits (which tend to straighten any curve) to obtain the Rényi dimensions.

Generalized dimensions $D(q)$ can be obtained with the method of moments for any image and box size described.

In order to compare the two multifractal analysis procedures involving either a single fractal measure for each of the intensity levels (or grouped in sets) with the moment calculation for the generalized dimensions, we checked the numerical values at each algorithm step. Outside of this scale range, the theoretical values of $D(q)$ (calculated as the limit when r approaches zero) and the numerical values of $D(q)$ (calculated from the regression fits) are still very close if we select the range of scale and a grid matching the theoretical generation pattern. We applied this for a range of oil spill images.

The study of the structured distribution in the space such that at any resolution the set is the union of similar subsets to the whole will indicate the same fractal dimension for every intensity value. But the scale factor at different parts of the set is not the same for most SAR images. If more than one dimension is needed, then the measure considered is characterized by the union of fractal sets, each one with a different fractal dimension.

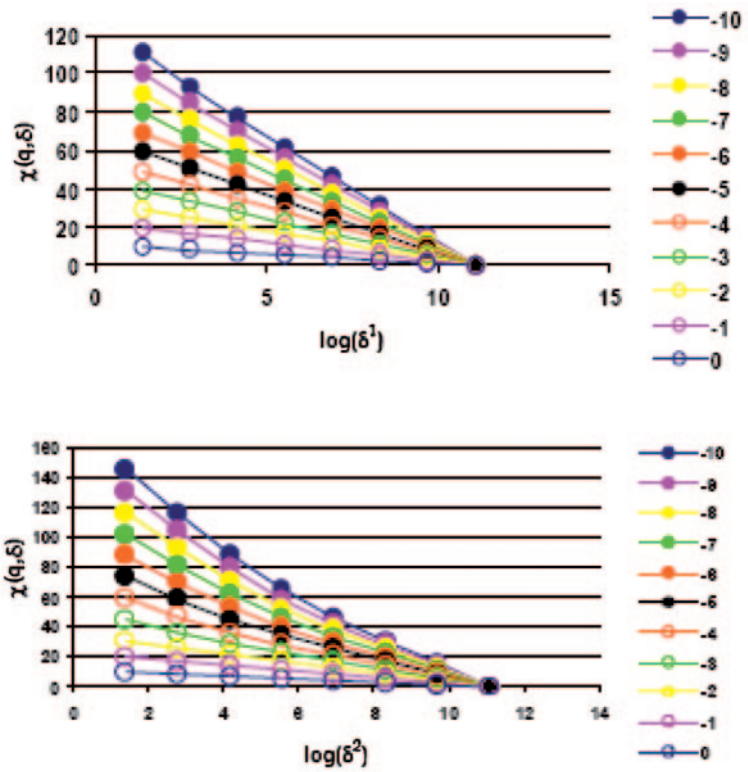

Fig. 5. – Range of functions $\chi(q, \delta)$ for a recent oil spill (top) and for a weathered one (bottom).

A modified partition function of all images for $0 = q = 10$ over box sizes e ranging from 1 to 512 pixels based on the square of the grey levels has been used. The mass exponent t is estimated as the slope of the log/log data for the SAR image showing the results for a recent and a dispersed oil spill for the optimized box size range in figs. 5 and 6.

Figures 5 and 6 show the different results applying the procedure described in subsect. **3**˙2 for both a recent and a weathered oil spill. Another possibility is to enhance the discrimination by concentrating on the highest valued pixels assigning them to the black SAR reflectivity values that correspond to the highest tensioactive concentrations on the ocean surface. The functions $\chi(q, \delta)$ are shown against the square or the cube of the intensity value, which improves the level of discrimination.

Figure 7 shows the comparison of the function $D(\rho)$ for a natural slick, that shows a smoother parabolic shape (squares) and a recent oil spill (dots) against a normalized SAR intensity, calculated by averaging over the background intensity values.

5. – Discussion

The SAR images exhibited a large variation of natural features produced by winds, internal waves, the bathymetric distribution, by thermal or solutal convection by rain, etc. as all of these produce variations in the sea surface roughness.

The satellite-borne SAR is able to detect oceanic features with a range of scales as

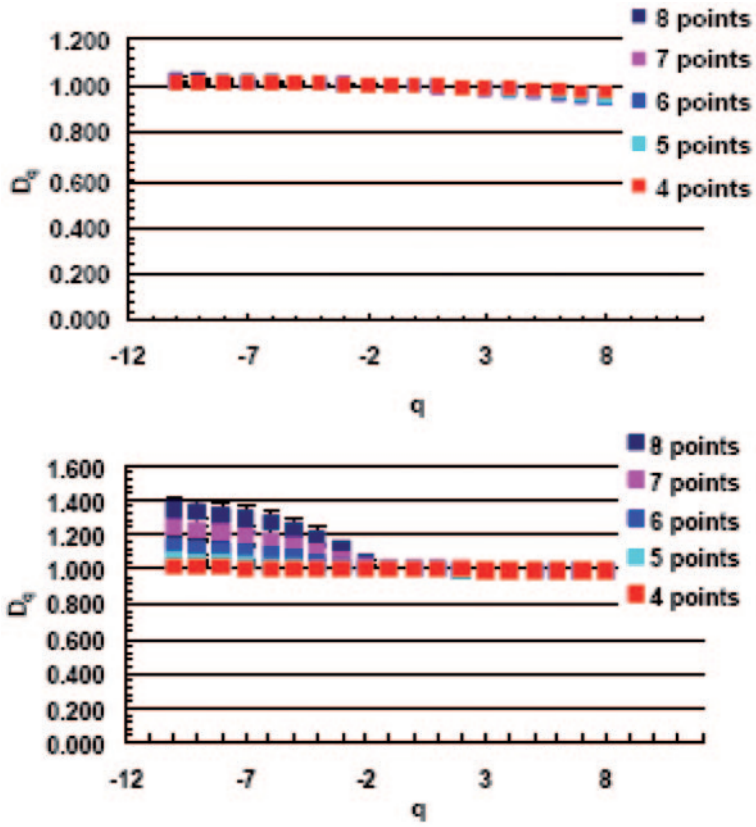

Fig. 6. – Generalized dimensions (D_q) obtained for a recent oil spill (top), showing the low values of the fractal dimension. A more weathered and convoluted oil spill (below) shows a more complex D_q set of functions.

seen in figs. 1 and 2, which shows several eddy structures in the Mediterranean, with a wide range of length scales. The spatial cross-correlation of the intensity signals may also give an indication of the length over which such features are correlated. Let $\rho(x)$ be the intensity of the SAR backscatter at point x and $\rho(x+\lambda)$ the intensity at a point separated by a distance λ from the first one. The normalised average

$$R(\lambda) = \frac{\langle \rho(x)\rho(x+\lambda)\rangle}{\langle \rho(x)^2\rangle} \tag{19}$$

represents the cross-correlation of $\rho(x)$ over the area where the average is taken. Dividing the average by the variance $V = \langle \rho^2 \rangle$ forces the value of $R(0)$ to be one.

The integral length scale associated to the sea surface roughness correlation is then defined in the usual way as

$$\lambda = \int_0^\infty R(\lambda)\mathrm{d}\lambda \tag{20}$$

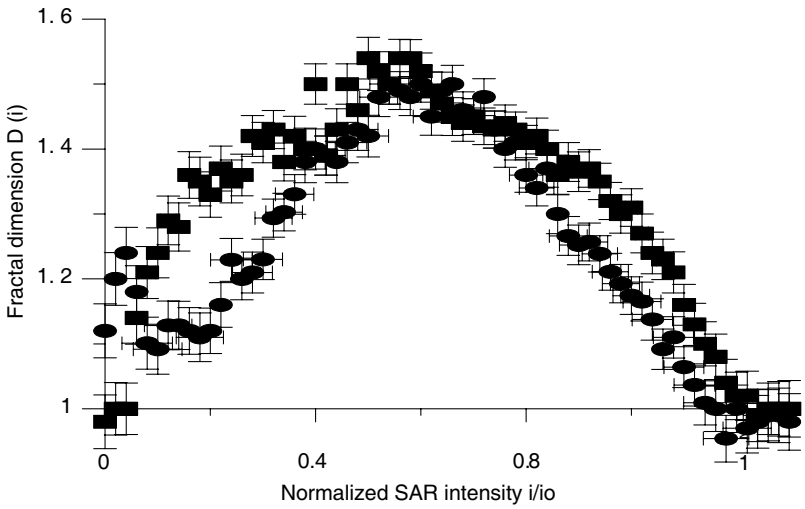

Fig. 7. – Multifractal set of dimensions $D(\mu)$ obtained for a recent oil spill (dots), showing the low values between 0.1 and 0.4 of the normalized SAR intensity. A natural spill is more convoluted (squares) and shows a more uniform parabolic type of $D(\mu)$ functions.

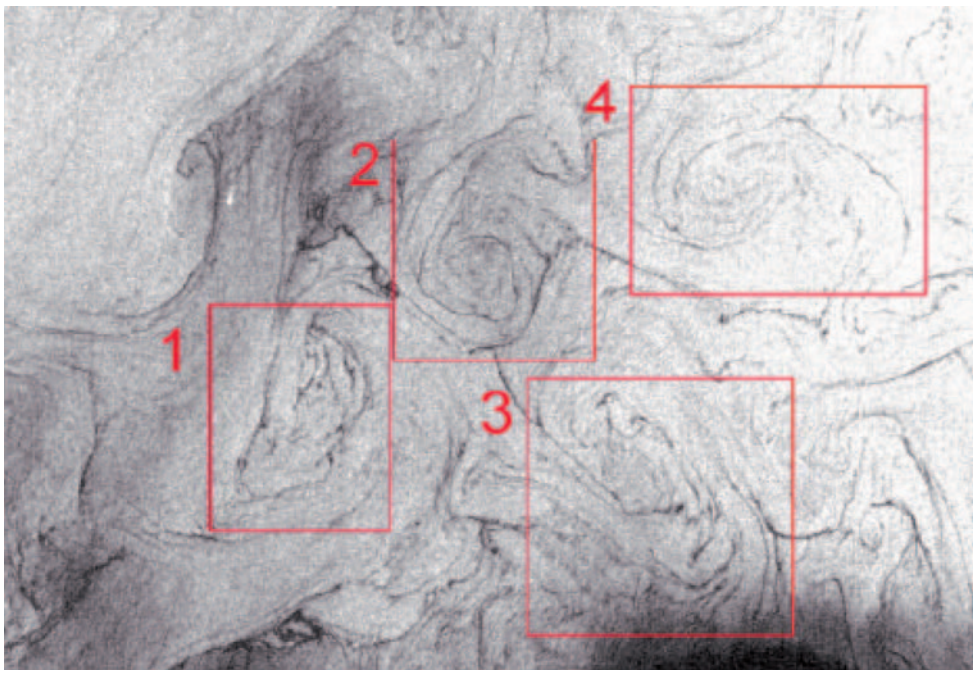

Fig. 8. – SAR intensity observations of 4 vortices in the ocean surface in the Mediterranean Sea.

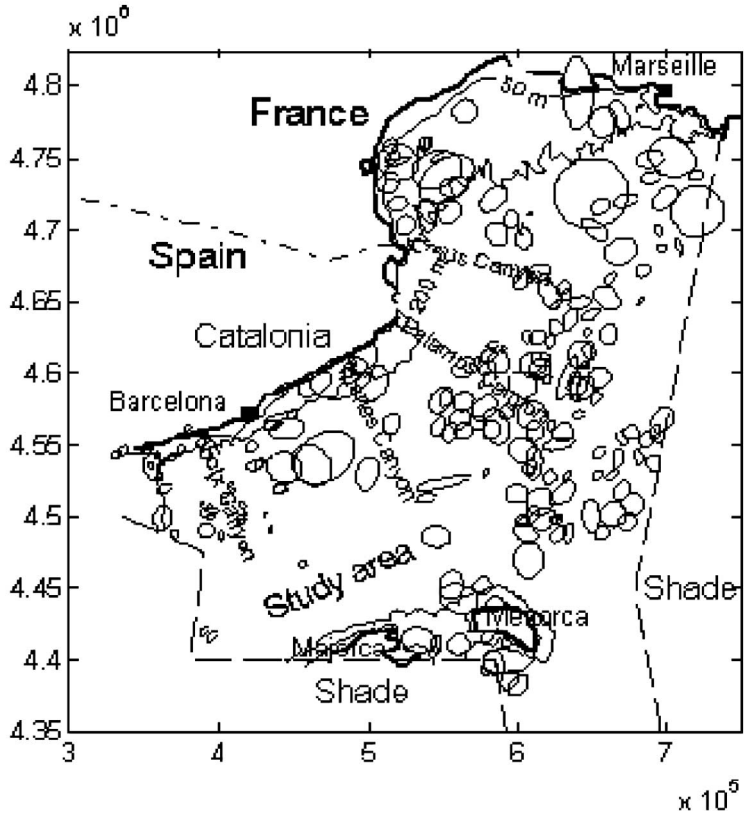

Fig. 9. – Detected shapes and sizes of the vortices detected during years 1997-1999 in the NW Mediterranean Sea.

which indicates the spatial scale l where the SAR intensities are well correlated. If we suppose that the surface currents are responsible (at least partly) for the spatial distribution of the ocean roughness for two main reasons, first the slope on both sides of an eddy is very different at producing radar backscatter from a side (as happens with ERS-1/2 and also ENVISAT), the other reason is that the surface tensioactives natural or man produced will be advected by the current lines relating the scalar and the vorticity distribution within the complex mesoscale ocean surface topology. Figure 8 shows an example of detected vortices using SAR. From the observations of a two-year period it is possible to map the positions, sizes orientations and shapes of a certain area as shown in fig. 9 for the region near Barcelona.

There is a very different type of SAR signature where convective cells are formed in the ocean surface, it is interesting to compare the multifractal appearance of the different signatures and this is shown for the examples in fig. 10, three vortices and a convective feature. The only quite different fractal structure is the bottom right one corresponding to the convective cells, where a clear plateau of a constant value of the maximum fractal dimension indicates that this measure is the same for the different intensity values of the SAR images. On the other hand, the vortical structures exhibit a slightly higher fractal value (1.6) for the higher SAR reflectivity (white) and a linear increase from the darker features (lines that indicate the eddy structure, mostly due to

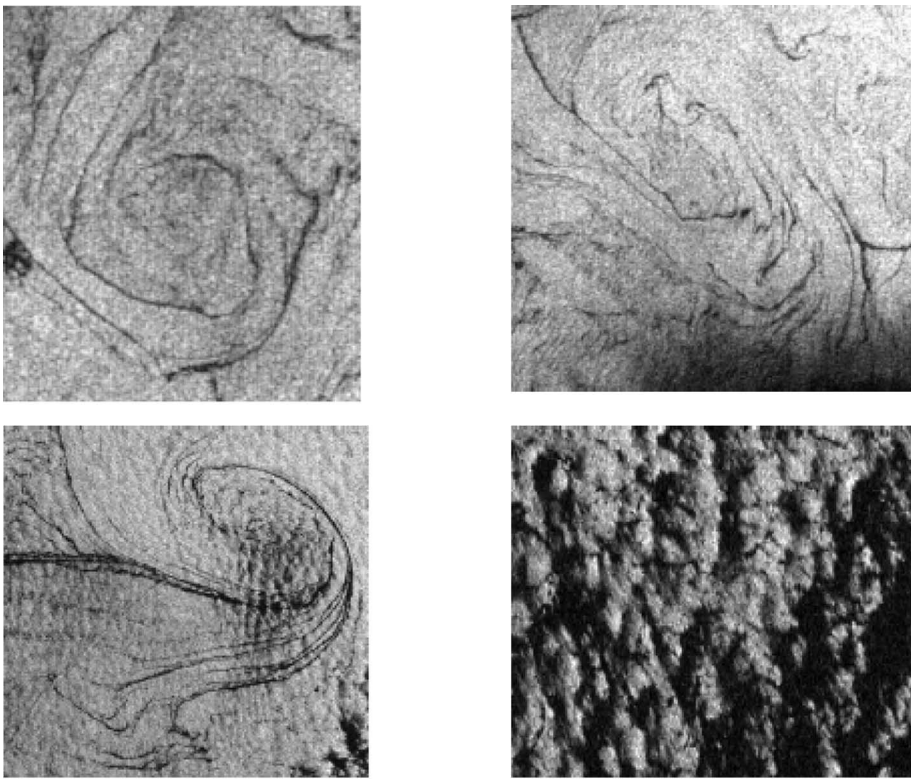

Fig. 10. – Comparison of four features in the ocean surface, a vortex in the top left corner and an area of convective activity in the right bottom corner, the other two cases have a combination of both features.

Langmuir convergence lines). It is obvious that the dark features, being elongated and smoother have a smaller fractal dimension than the background area between the spiral structures. But the appearance of a linear increase is not clear. The fact that convective structures take place in all the images and the structures are marked both by darker (meaning a smooth surface) and white (rougher sea surface areas) zones explains that at a wider range the maximum fractal dimension (D) is about the same (1.55) as seen in fig. 11 for convective cells. Figure 12 shows a typical multifractal plot for an ocean surface feature driven by internal waves, while fig. 13 shows $D(\rho)$ for a weathered oil spill.

The geometrical-dynamical equivalences described above may be used to check different methodologies of fractal dimension calculations. When the spectra can be written as a function of an on/off scalar quantity, it is also possible to directly relate the fractal dimension with the spectra as described above, although there are still several arguments leading to different relationships [29]. Also the possibility of a small-scale (sub grid or sub interrogation/pixel region) turbulent diffusion exists. The appearance of a set of scalar values, such as the SAR radar backscattered reflectivity as a superposition of on/off contours which may not be connected to a set of continuous values makes the geometrical appearance of the environmental flow much more complicated but more realistic.

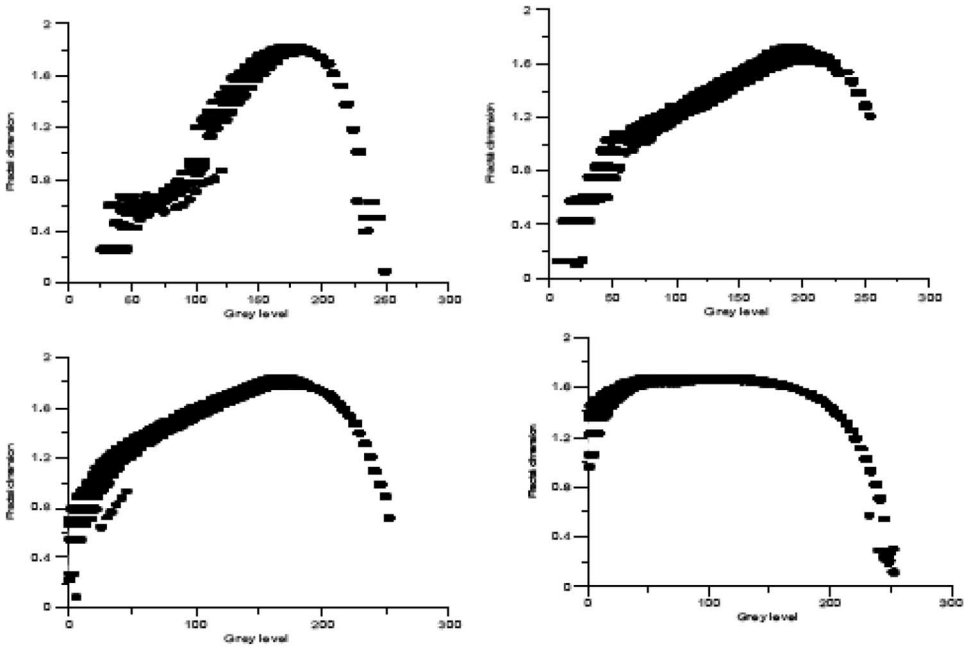

Fig. 11. – Comparison of the multifractal $D(\rho)$ plots for the four features in the ocean surface shown in fig. 9 a vortex in the top left corner, with a parabolic shape, and an area of convective activity in the right bottom corner, with a uniform value of D over a wide range of SAR intensity values, the other two cases have a combination of both features.

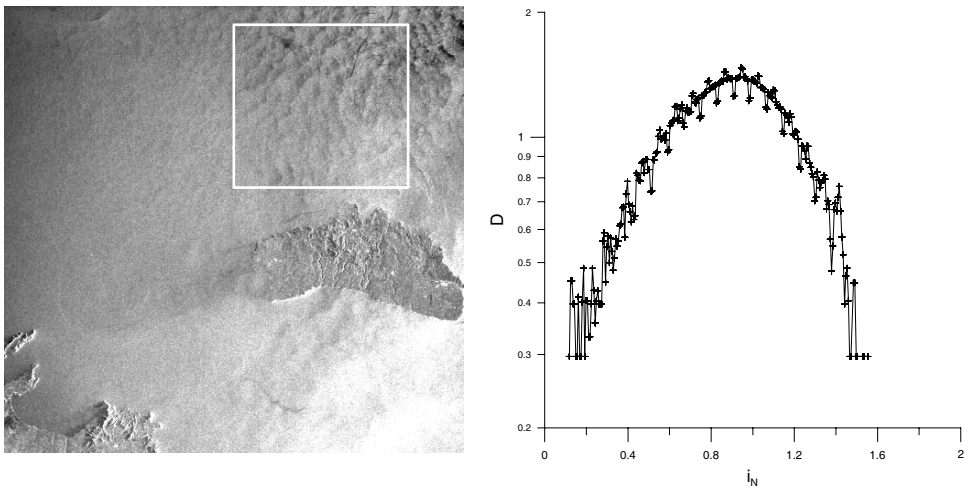

Fig. 12. – Multifractal $D(\rho)$ plot for a region of internal waves detected by SAR, with a parabolic shape, and a maximum value of D of 1.4.

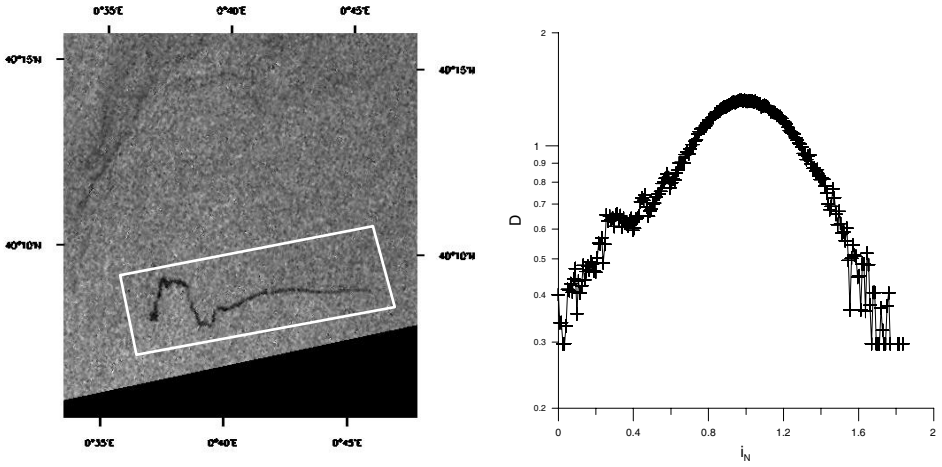

Fig. 13. – Multifractal $D(\rho)$ plot for a weathered oil spill detected by SAR, showing a combination of the parabolic shape, with some skewness and low values at low SAR reflectivity and a maximum value of D of 1.4.

6. – Conclusions

The use of routine satellite information by SAR or other sensor types may be of great interest to build a seasonal database of the dynamic conditions of the mesoscale turbulence in the ocean, after several years of observations the dominant patterns and the causes for different topological characterisations might be understood better [29, 30].

In the simplified conditions described above the maximum size of stable vortices can be characterized directly by the Rossby deformation radio R_D depending on the square root on the depth on the local thermocline h. There is self-similar scaling at a very large range of scales and a linear dependence between the R_D and the frequency of Brunt-Väisälä in the condition of a fixed h, this may be used to forecast and to check from satellite routine observations many of the dynamic characteristics of a certain area. The strong vertical stratification of the surface water aids the development of the largest vortices. As the frequency N strongly depends on the seasonal thermal balance, the wave mixing activity and other local bathimetry induced processes that affect the water column, the range and spatial distribution of detected vortices is very useful in the predictive behaviour of a marine zone.

The use of thematic maps that may be updated from combined satellite sensors and images and validated with space *in situ* observations may be even used to predict local diffusion. In such a manner, more sophisticated data analysis such as the evaluation of integral length scales or local fractal dimensions of the sea surface appearance, together with the detailed information of the position and sizes of the mesoscale dominant eddies of size about R_D provides useful information on the mesoscale ocean turbulence.

A large collection of more than 900 SAR images obtained from three European coastal areas (Baltic Sea, North Sea and NW Mediterranean) by the ERS-1 and ERS-2 were analyzed and compared with other Satellite images. The research was done in the frame-

work of the CLEAN SEAS European Union project and more information is available at [13-16].

The use of routine satellite information by SAR or other sensor types may be of great interest to build a seasonal database of the dynamic conditions of the mesoscale turbulence in the ocean, after several years of observations the dominant patterns and the causes for different topological characterisations might be understood. It is important to characterize the types and structure of the main vortices detected as well as the spectral cascade processes that take place, these may be investigated by using fractal methods on images of the area as well as with models of the turbulent cascade and field measurements of diffusion [30-32].

The different multifractal formalisms can be used to discriminate between different physical processes that, despite being similar, have different transport mechanisms for the different scales, or in time. From the comparison of the multifractal plots of the well-defined SAR detected vortices with those of convective cells, vortices show a maximum complexity for the low reflectivity values, while convection, probably because the basic instability happens everywhere at the same time, exhibits almost the same fractal dimension for a wide range of intermediate SAR reflectivity. The analysis of recent *versus* more convoluted oil spills is also interesting both in the formalisms presented in subsect. **3**˙2 and **3**˙3. The recent oil spills pave a well-defined spatial and temporal origin, so as time develops (measured in terms of the turbulence of the area) the fractal measures tend to be those of the turbulent environment, initially for low SAR reflectivity the generalised dimensions are low but in time they increase to a limit of 1.5–1.6.

* * *

This work was supported by the Ministerio de Educación y Ciencia of Spain and the Universitat Politècnica de Catalunya (RYC-2003-005700, FTN-2001-2220, ESP2005-07551). Authors also acknowledge the CLEAN SEAS (ENV4-CT96-0334) European Union Project and the ESA (AO-ID C1P.2240) for the SAR images provided.

REFERENCES

[1] Munk W., *Sciencia Marina*, **65** (2001) 193.
[2] Turcotte D. L., *Annu. Rev. Fluid Mech.*, **20** (1988) 5.
[3] Feder J., *Fractals in Physics* (Cambridge University Press, Cambridge) 1988.
[4] Richardson L. F., *Proc. R. Soc. London, Ser A*, **110** (1926) 709.
[5] Kolmogorov A. N., *C. R. Acad. Sci. USSR*, **30** (1941) 301.
[6] Kolmogorov A. N., *J. Fluid Mech.*, **13** (1962) 82.
[7] Kraichnan R., *Phys. Fluids*, **10** (1967) 1417.
[8] Gade M. and Alper W., *Sci. Total Environ.*, **237/238** (1999) 441.
[9] Gade M. and Redondo J. M., *Marine pollution in European coastal waters monitored by the ERS-2 SAR: a comprehensive statistical analysis. IGARSS 99. Hamburg*, Vol. **III** (1999), p. 1239.
[10] Grau J., *Analysis of the Meteosat images sequences using the digital processing method*. PhD Thesis UPC, Barcelona (2005).
[11] Platonov A. K., *SAR satellite images applications to both sea contamination and dynamic studies in the NW Mediterranean*, PhD Thesis, UPC Barcelona (2002), `http://www.tdcat.cesca.es/TDCat-0905102-135541/`.
[12] Redondo J. M. and Platonov A. K., *Environ. Res. Lett.*, **4** (2009) 14008.
[13] Redondo J. M. and Platonov A., *Ing. Agua*, **8** (2001) 15.
[14] Zouari N. and Babiano A., *Phys. D*, **76** (1994) 318.

[15] Linden P. F., Boubnov B. M. and Dalziel S. B., *J. Fluid Mech.*, **298** (1996) 81.
[16] Carrillo A. A., Sanchez M. A., Platonov A. and Redondo J. M., *Phys. Chem. Earth B*, **26** (2001) 305.
[17] Chen X. and Allen S. E., *J. Geophys. Res.*, **101** (1996) 18043.
[18] Mahjoub O. B., Redondo J. M. and Babiano A., *J. Flow Turbul. Combust.*, **59** (2000) 299.
[19] Seuront L., Schmitt F., Lagadeuc Y., Schertzer D. and Lovejoy S., *J. Plankton Res.*, **21** (1999) 877.
[20] Bezerra M. O., Diez M., Medeiros C., Rodriguez A., Bahia E., Sanchez-Arcilla A. and Redondo J. M., *J. Flow Turbul. Combust.*, **59** (1998) 191.
[21] Mandelbrot B. B., *Physica Scripta*, **32** (1985) 257.
[22] Redondo J. M. and Linden P. F., *Geometrical Observations of Turbulent Interfaces: The Mathematics of Deforming Surfaces* (IMA, Clarendon Press, Oxford) 1996.
[23] Vassilicos J. C. and Hunt J. C. R., *Proc R. Soc. London, Ser A.*, **435** (1991) 505.
[24] Dubucm B., Zucker S. W., Tricot C., Quiniou J. F. and Wehbi D., *Phys. Rev. A*, **425** (1989) 113'27.
[25] Evertsz C. J. G. and Mandelbrot B. B., *Multifractal measures*, in *Chaos and Fractals: New Frontiers of Science*, edited by Peitgen H., Jurgens H. and Saupe D. (Springer-Verlag, NY) 1992, pp. 921-953.
[26] Plotnick R. E., Gardner R. H., Hargrove W. W., Prestegaard K. and Perlmutter M., *Phys. Rev. E*, **53** (1996) 5461.
[27] Rényi A., *Acta Math. Hung.*, **VI** (1955) 285.
[28] Stanley H. and Meakin P., *Nature*, **335** (1988) 405.
[29] Redondo J. M., *Mixing efficiency of different kinds of turbulent processes and instabilities. Applications to the environment*, in *Turbulent Mixing in Geophysical Flows*, edited by Linden P. F. and Redondo J. M. (CIMNE, Barcelona) 2002, pp. 131-157.
[30] Berrizi F., Dalle Mese E. and Martorella M., *Int. J. Remote Sens.*, **25** (2004) 1265.
[31] Fung J. C. H., Hunt J. C. R., Malik N. A. and Perkins R. J., *J. Fluid Mech.*, **236** (1992) 281.
[32] Rodriguez A., Sanchez-Arcilla A., Redondo J. M., Bahia E. and Sierra J. P., *Water Sci. Technol.*, **32** (1995) 169.